JOURNAL OF SOLID STATE CHEMISTRY 56, 203–210 (1985)

Small-Defect Clusters in Chromia-Doped Rutiles

L. A. BURSILL

School of Physics, University of Melbourne, Parkville, 3052, Victoria, Australia

DAVID J. SMITH

High-Resolution Electron Microscope, University of Cambridge, Free School Lane, Cambridge, CB2 3RQ, England

AND PENG JU LIN

Physics Department, Nanking University, Nanking, China

Received May 14, 1984; in revised form July 30, 1984

Bright-field phase contrast electron microscope images of chromia-doped rutiles have been used to study the size and distribution of small defect clusters in specimens of TiO_2, $(Ti,Cr)O_{1.995}$, and $(Ti,Cr)O_{1.985}$. Comparisons of observed and measured spot contrast densities, and contrast calculations using computer simulations of the defect structures, lead to the conclusion that the smallest clusters observed contained ~32 Cr^{3+} cations. Larger clusters occurred with increasing frequency for higher dopant levels, which is consistent with increased interaction and aggregation of traditional or reconstructed small defects (e.g., Cr^{3+} interstitials or charge-compensated oxygen vacancies).

1. Introduction

Phase analysis studies have shown that up to 7.5 mole% $CrO_{1.5}$ may be retained in TiO_2, at 1770 K, without observable precipitation of extended defects, such as crystallographic shear planes (CSP). The net anion deficiency is presumably accommodated as randomized small-defect complexes (*1, 2*). *In situ* electron microscopy complemented by *ex situ* furnace heating experiments (*3*) established the precipitation and dissolution temperatures for small/extended defect equilibria, allowing the phase limits to be determined directly. For low dopant levels (≤500 ppm) the appropriate small defect appears to be a reconstructed oxygen vacancy (*4*), containing one pair of face-sharing $[CrO_6]$ octahedra. For higher dopant levels, structural considerations and HREM evidence support a linear cationic interstitial model, containing two pairs of $[CrO_6]$ face-sharing octahedra (*3, 5*).

Computer simulations for both traditional point defect models (i.e., oxygen vacancies or Ti^{4+} interstitials) and for the re-

0022-4596/85 $3.00

constructed interstitial and vacancy defects predicted that individual small defects should give observable contrast for [100] and [001] zone axis images of rutile, provided that strong Bragg beams did not contribute to the image (Figs. 7, 8 of Ref. (*6*)). The contrast should be strongly thickness-dependent and the Scherzer optimum defocus condition should be used for maximum contrast. It was suggested that chemically thinned wedge-shaped crystals offer the best chance for positive detection and even identification of small defects, when the predicted thickness dependence of the contrast and the projected density distribution of small defects should allow artifact contrast due to surface steps or contamination to be distinguished.

High-resolution phase contrast observations of small defects in pure and chromia-doped rutile are presented below. These are the first application of the predictions of Ref. (*6*) in order to observe small defects by high-resolution phase contrast electron microscopy. Even though individual small defects have not been definitively identified or located, it is clear that the images at least represent the distribution of small-defect clusters within nonstoichiometric (Ti,Cr) O_{2-x} ($0 \leq x \leq 0.02$).

2. Experimental

Specimens were prepared starting with a single-crystal boule of rutile, sliced into sections normal to [100]. Chromia powder was weighed and loaded onto a slice to give overall stoichiometrics (Ti,Cr)O_{2-x} ($x = 0$, 0.005, and 0.015). The slices were carefully wrapped in platinum foil and then heated at 1773 K for 2 days. The foils were then cooled rapidly (within ca. 1 m) to room temperature, by placing them in contact with a metal block, after removal from the furnace.

Thin sections parallel to (010) were then cut with a diamond saw and mechanically polished to thickness $\simeq 50$ μm. Almost uniform reddish-brown colorations indicated there were no gross variations in dopant concentration. The sections were then chemically thinned using $KHSO_4$ solution (0.1 *m*) at 753–873 K. In this way essentially strain-free wedge-shaped specimens were obtained, which were well suited to the present experiments.

High-resolution images were obtained with the Cambridge University 600 kV HREM (*7*). The crystal wedges were tilted so that [010] was parallel to the electron beam. Usually, the high-resolution, high-magnification image was then observed allowing incident-beam alignment and astigmatism corrections to be made. Finally, a small objective aperture was inserted ($\mathbf{d} \geq$ 3.3 Å) to exclude Bragg diffracted beams. Bright-field images were recorded at magnifications (~150,000×) sufficient to reveal the thickness variation of any small-defect contrast. Some observations (Fig. 2b) of small defects in (nominally) pure rutile were also made with the JEOL 200CX instrument at Centre d'Energie Nucléaire (Grenoble).

3. Observations

Figure 1 shows typical examples of [010] bright-field images of TiO_2, (Ti,Cr)$O_{1.995}$, (Ti,Cr)$O_{1.985}$, and (Ti,Fe)$O_{1.98}$ specimens, recorded with objective aperture cutoff of about 3.3 Å. These images have all been reproduced with identical linear scales and exhibit approximately equivalent wedge angles. There are no visible defects for TiO_2 (a) but spot contrast appears with increasing density, size, and frequency for increasing dopant levels (b, c). It is important to note that the small-defect density apparently increases for increasing specimen thickness which is consistent with the presence of an approximately uniform *bulk,* rather than *surface,* density of small imaged objects. Figure 1d shows the corresponding

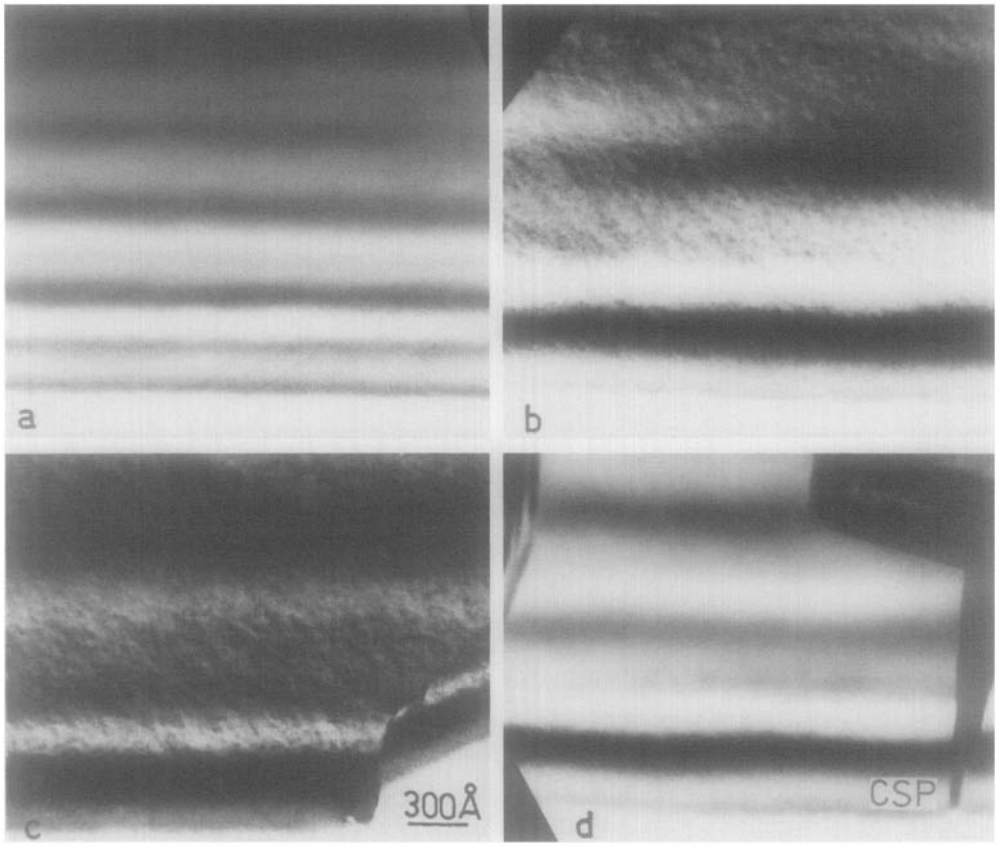

FIG. 1. Bright-field phase contrast images of nominally pure TiO_2 (a), $(Ti,Cr)O_{1.995}$ (b), $(Ti,Cr)O_{1.985}$ (c), and $(Ti,Fe)O_{1.98}$ (d). Samples (b) and (c) were quenched from 1500°C whereas (d) had been cooled slowly so that extended defects precipitated. Note absence of spot contrasts in (a) and (d) and increasing density of spot contrasts in (b) and (c).

image for a specimen of $(Ti,Fe)O_{1.98}$ which had been annealed outside the nonstoichiometric phase limits. In this case, small defects have been precipitated as extended defects (CSP). The absence of visible spot contrast apparently confirms this expectation (cf. Fig. 1a).

Figures 2a, b show enlargements of similar images obtained from TiO_2 and $(Ti,Cr)O_{1.995}$ specimens having relatively shallow wedge angles. These two images were chosen as examples for more detailed analysis since they are relatively free of surface "contamination" layers and both were recorded at objective lens defocus close to Scherzer. Note the relatively low density of spot-contrast features for TiO_2 with a much higher density for $(Ti,Cr)O_{1.995}$. These spots contrast are apparently randomly distributed. In each case the black-spot contrasts and sizes are approximately the same, and are ~5–15 Å in diameter. The apparent density of spots increases significantly on crossing from the first extinction contour (bottom of Fig. 2a) to the second (top of Fig. 2a), again implying that the defects are predominantly bulk features rather than surface artifacts. The contrast level for the small defects is estimated to be 5 ~ 15% relative to background and much lower

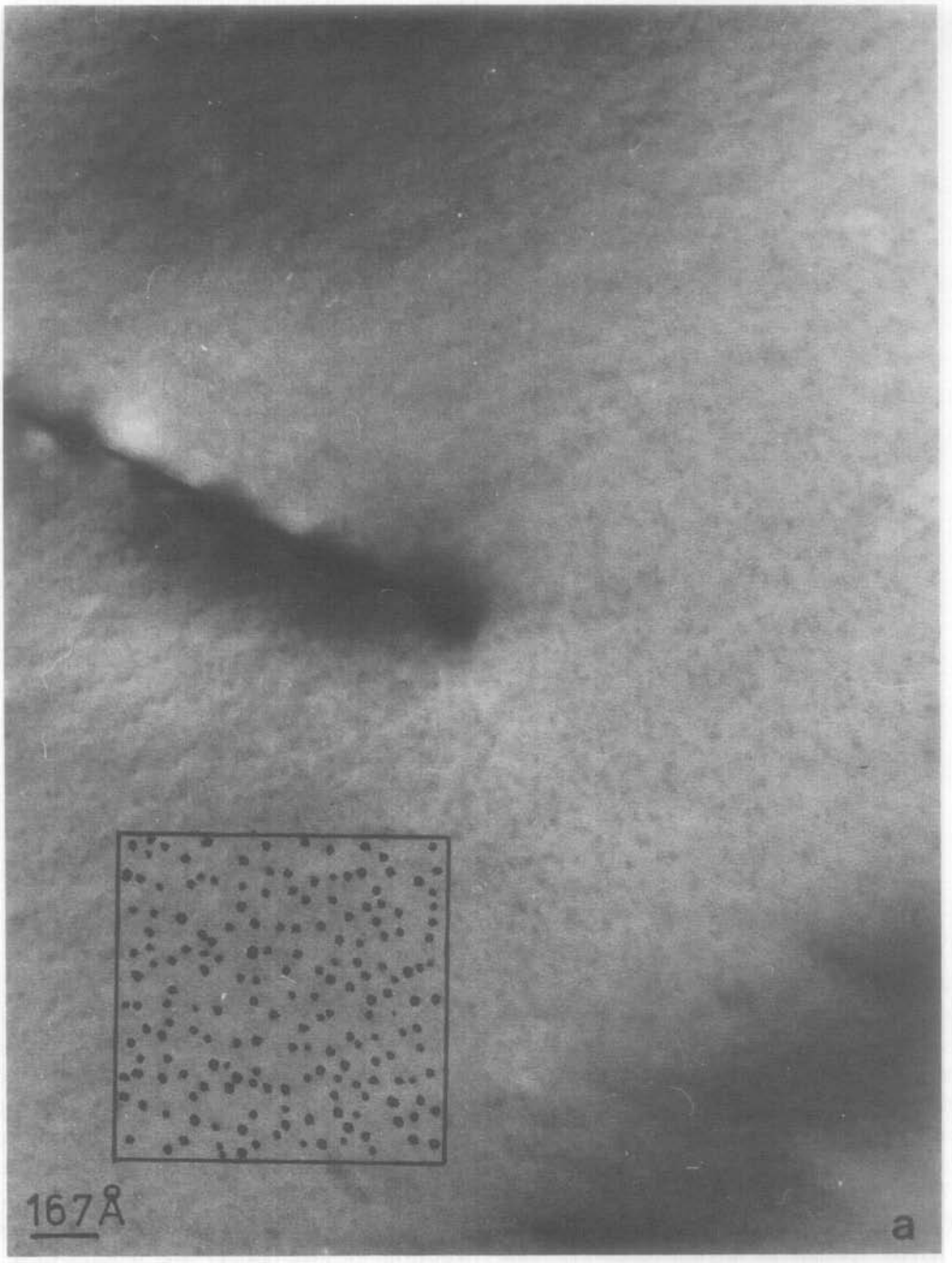

FIG. 2. Bright-field phase contrast image from specimens of $(Ti,Cr)O_{1.995}$ (a) and nominally pure TiO_2 (b), with relatively shallow wedge angles. Squares indicate regions used for spot-contrast density measurement. Note increase in density of spots on crossing from first (bottom) to second (top) thickness extinction contour in (a).

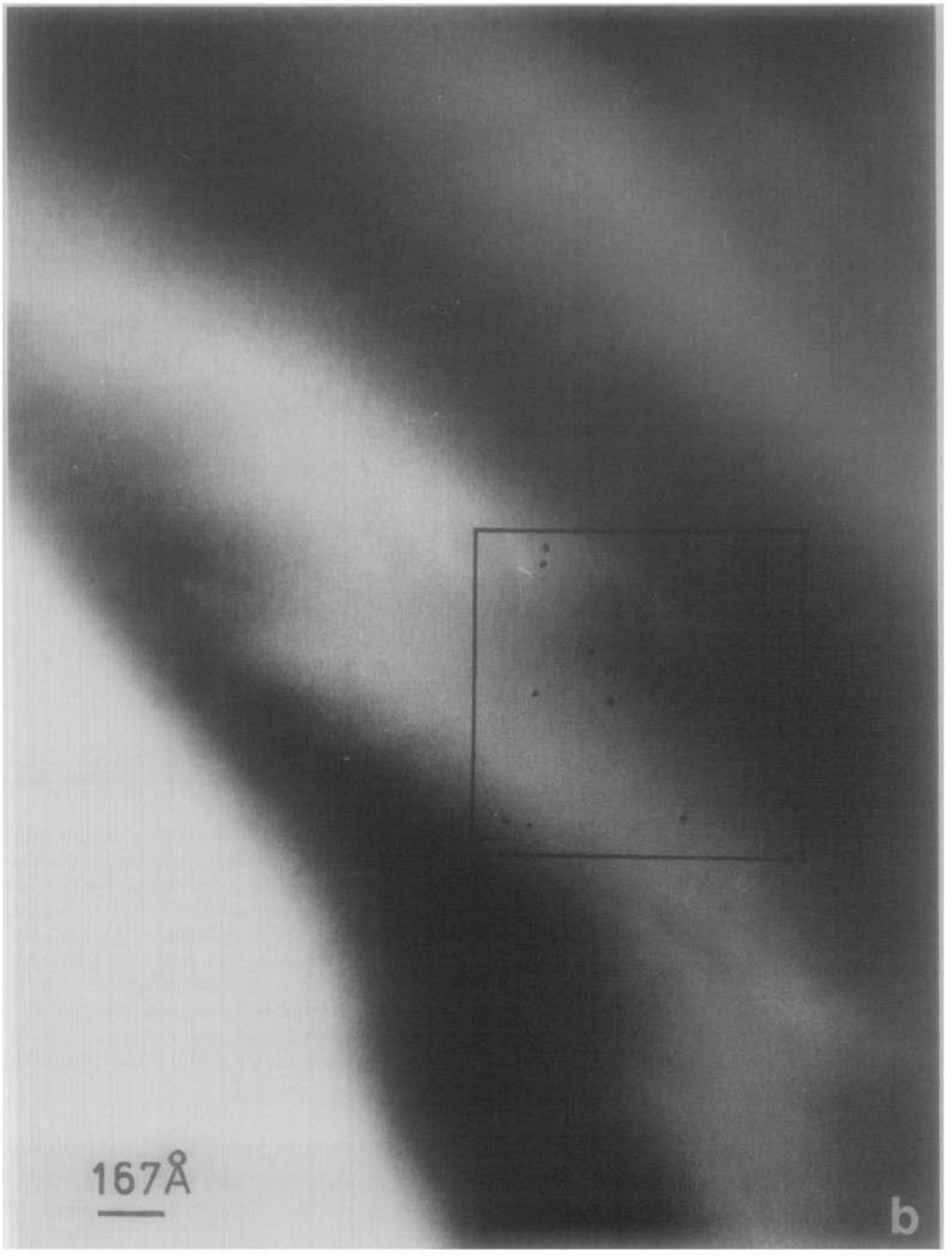

FIG. 2—*Continued.*

than diffraction contrast from a (100) platelet defect imaged by diffraction contrast in Fig. 2a. Small-defect contrast reaches a maximum within the second thickness extinction contour (cf. Fig. 3a below). Note the asymmetrical distribution of small defects about the (100) platelet defect.

4. Discussion

(*a*) *Structure of small defects and image calculations*. The structural models, principles for individual small-defect visibility, and computational techniques have already been described (*4–6*). Figures 3a and b show the essential results required for understanding the observed thickness variation of small-defect contrast. Plots of visibility (*V*, see Ref. (*6*) for definition) versus thickness (*H*, Å) for reconstructed and traditional vacancy and interstitial models for the [010] projection of rutile (Fig. 3a) show that the maximum visibility (15–20%) coincides with the thickness extinction contour at ca. 200 Å thickness (500 kV electrons) but remains above the detection limit (3–5%) for most thicknesses. Smaller maxima in visibility occur at higher order thickness extinction contours (not shown in Fig. 3a). Note that the (realistic) reconstructed small-defect models should be readily visible whereas the traditional interstitial and vacancy models are probably below the detection limit for this projection. Figure 3b compares visibility versus thickness for superimposed linear interstitial defects. Note that the maximum contrast is increased remarkably from 20% for one defect to 72% for six defects. Thus any tendency for defect aggregation (cluster formation) should give a marked increase in visibility.

(*b*) *Expected densities of small defects*. Table I lists the calculated mean *linear* separation expected for small-defect clusters corresponding to the stoichiometries examined here. Note that whereas oxygen vacancies have two associated Cr^{3+} cations

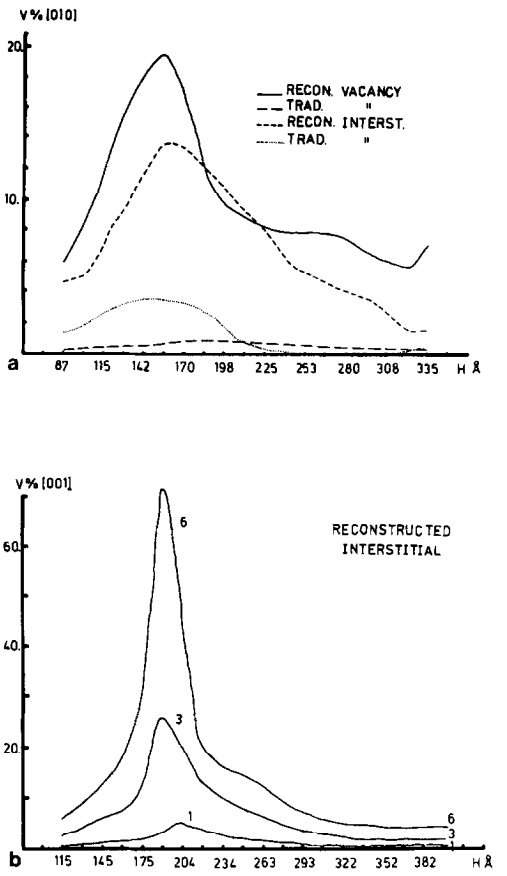

FIG. 3. (a) Plots of visibility (*V*) versus thickness (*H*) for reconstructed and traditional vacancy and interstitial models for [010] projection of rutile (500 kV). Note detectable visibility levels (≥5%) for reconstructed models for $85 \leq H \leq 308$ Å thickness (see Ref. (*6*)). (b) Comparison of visibility (*V*) versus thickness (*H*) for superimposed linear interstitial defects for rutile. Note that maximum visibility is increased from 20 to 72% (at $H = 200$ Å) for six defects, and corresponding increase in specimen thickness range over which defects should be visible.

the traditional and reconstructed interstitial defect models have one and four associated Cr^{3+} cations per defect, respectively. The mean *projected* separations are given in Table II, for crystal thicknesses of 100, 200, and 400 Å. Note that the mean separation of Cr^{3+} ions is only 9.2 Å for $(Ti,Cr)O_{1.98}$, 14.6 Å for $(Ti,Cr)O_{1.995}$, and is only 68 Å in nominally pure TiO_2. For 200-Å-thick crys-

TABLE I

MEAN LINEAR SEPARATION OF DEFECT CLUSTERS IN RUTILE

Specimen stoichiometry	Mean linear separation (Å) of Cr^{3+} clusters						
	$1Cr^{3+}$ (Trad. interstitial)	$2Cr^{+}$ (Vacancy)	$4Cr^{3+}$ (Linear interstitial)	$8Cr^{3+}$	$16Cr^{3+}$	$32Cr^{3+}$	$64Cr^{3+}$
TiO_2 (nominal purity 100 ppm)	67.8	85.4	108.1	135.6	170.9	215.3	271.3
$(Ti,Cr)O_{1.995}$	14.6	18.4	23.2	29.2	36.8	46.35	58.4
$(Ti,Cr)O_{1.98}$	9.2	11.6	14.2	18.4	23.2	29.2	36.8

tals, corresponding to the thickness where we expect maximum visibility, the mean projected separation is only 3.9 Å for $(Ti,Cr)O_{1.995}$. It would therefore be surprising if there were not considerable clustering present in these samples, especially $(Ti,Cr)O_{1.985}$. Note that even the pure sample should show a readily detectable density of small-defect contrasts.

(*c*) *Assessment of experimental images.* The variation of density of spot contrast seen in Figs. 1a–c is qualitatively in agreement with the stoichiometry of the samples. The contrast variations with increasing thickness are also in qualitative agreement with the computer simulations, with lower contrast in the bright thickness contours. Figures 2a and b appear to be more suitable for spot-contrast density measurements. Spot-counting in a 800 × 800-Å square yields a mean projected defect separation of ≃60 Å for $(Ti,Cr)O_{1.995}$ and ≃170 Å for TiO_2 (nominally pure). The wedge angles and topologies of Figs. 2a and b do not allow the crystal thickness to be determined readily, for example, by comparison with calculations of transmitted beam intensity versus thickness (cf. Figs. 1a, b, and d and Fig. 4a of Ref. (*6*)). However, following comparison with Tables I and II, we expect that spot contrasts observed in, e.g., Figs. 1b, c, and 2b would represent *clusters,* rather than individual small defects, with the clusters containing 64 → 256 Cr^{3+} at-

TABLE II

MEAN PROJECTED SEPARATION OF DEFECT CLUSTERS IN RUTILE

Specimen stoichiometry	Specimen thickness, Å	Mean projected separation (Å)						
		$1Cr^{3+}$	$2Cr^{3+}$	$4Cr^{+}$	$8Cr^{3+}$	$16Cr^{3+}$	$32Cr^{3+}$	$64Cr^{3+}$
TiO_2 (nominal purity 100 ppm)	100	55.9	78.9	111.6	158	223	316	447
	200	39.5	55.9	78.9	112	158	223	316
	400	27.9	39.5	55.9	79	112	158	223
$(Ti,Cr)O_{1.995}$	100	5.5	7.9	11.2	15.8	22.3	31.6	44.6
	200	3.9	5.6	7.9	11.2	15.8	22.3	31.6
	400	2.8	3.9	5.6	7.9	11.2	15.8	22.3
$(Ti,Cr)O_{1.98}$	100	2.8	3.9	5.6	7.9	11.2	15.8	22.3
	200	2.0	2.8	3.9	5.6	7.9	11.2	15.8
	400	1.4	2.0	2.8	3.9	5.6	7.9	11.2

oms, depending on whether the crystal thickness is, e.g., 200 or 400 Å. Since the observable spot contrasts of Fig. 2b, for the nominally pure TiO_2 specimen, have levels comparable with that in Fig. 2a, then, even here, it seems that only clusters of impurity atoms may have been imaged successfully.

(*d*) *Limitations of present experiments.* A severe problem was the thin amorphous surface layer covering most specimens which was presumably formed during the period (~1 week) between sample preparation and actual observation. This effectively eliminated any chance of seeing individual small defects containing, for example, fewer than ~16–32 Cr^{3+} atoms (i.e., 4–8 linear interstitial defects). *In situ* cleaning of specimens and ultrahigh vacuum specimen chambers may help overcome this problem in future work. A second limitation, preventing quantitative measurement of cluster density, was the lack of control achieved over wedge angle and crystal thickness. Severe problems also arise over correct choice of exposure times for recording the images, especially for those from the predicted high-contrast region of ~200 Å thickness. Photographic printing to reveal the range of contrasts seen on the negatives is difficult. Where clusters show a range of contrast levels there are some difficulties over deciding whether or not a given spot should be counted. Errors of ~3× could readily occur in estimating spot densities.

Conclusion

Bright-field phase-contrast images of chromia-doped rutiles have been obtained which probably represent the distribution of small-defect clusters (containing ≥32 Cr^{3+} atoms, equivalent to >8 linear defects) in a specimen of $(Ti,Cr)O_{1.995}$. Even larger clusters appear for $(Ti,Cr)O_{1.985}$ (Fig. 1c), as indicated by comparison of contrast levels and spot separations with calculations. The analyses of Tables I and II would clearly require clustering to occur for $(Ti,Cr)O_{1.985}$ and the observations suggest this also occurs in $(Ti,Cr)O_{1.995}$, and even nominally pure TiO_2.

Acknowledgments

This work was supported by the Australian Research Grants Committee, the Universities of Melbourne and Nanking and the Science and Engineering Research Council (U.K.). DJS is grateful to the University of Melbourne for support of a 2-month visit to the School of Physics.

References

1. L. A. Bursill and Shen Guang Jun, *J. Solid State Chem.* **51,** 388 (1984).
2. D. K. Philp and L. A. Bursill, *J. Solid State Chem.* **10,** 357 (1974).
3. L. A. Bursill, M. G. Blanchin, and D. J. Smith, *Philos. Mag.*, in press.
4. L. A. Bursill and M. G. Blanchin, *J. Solid State Chem.* **51,** 321 (1984).
5. L. A. Bursill and M. G. Blanchin, *J. Phys. Lett. (Orsay, Fr.)* **44,** L165 (1983).
6. L. A. Bursill and Shen Guang Jun, *Optik* **66,** 251 (1984).
7. D. J. Smith, R. A. Camps, V. E. Cosslett, L. A. Freeman, W. O. Saxton, W. C. Nixon, H. Ahmed, C. J. D. Catto, J. R. A. Cleaver, K. C. A. Smith, and A. E. Timbs, *Ultramicroscopy* **9,** 203 (1982).